

# Investigating deformable image registration and scatter correction for CBCT-based dose calculation in adaptive IMPT

Christopher Kurz<sup>a)</sup>

*Department of Radiation Oncology, LMU Munich, Munich 81377, Germany and Department of Medical Physics, Ludwig-Maximilians-Universität München, Garching bei München 85748, Germany*

Florian Kamp

*Department of Radiation Oncology, LMU Munich, Munich 81377, Germany*

Yang-Kyun Park

*Department of Radiation Oncology, Massachusetts General Hospital and Harvard Medical School, Boston, Massachusetts 02114*

Christoph Zöllner

*Department of Medical Physics, Ludwig-Maximilians-Universität München, Garching bei München 85748, Germany*

Simon Rit

*Université de Lyon, CREATIS, CNRS UMR5220m Inserm U1044, INSA-Lyon, Université Lyon 1, Lyon F69373, France*

David Hansen

*Department of Oncology, Aarhus University Hospital, Aarhus 8000, Denmark*

Mark Podesta

*Department of Radiation Oncology (MAASTRO), GROW-School for Oncology and Developmental Biology, Maastricht University Medical Centre, Maastricht 6229 ET, The Netherlands*

Gregory C. Sharp

*Department of Radiation Oncology, Massachusetts General Hospital and Harvard Medical School, Boston, Massachusetts 02114*

Minglun Li, Michael Reiner, Jan Hofmaier, Sebastian Nepl, Christian Thieke, Reinoud Nijhuis, Ute Ganswindt, and Claus Belka

*Department of Radiation Oncology, LMU Munich, Munich 81377, Germany*

Brian A. Winey

*Department of Radiation Oncology, Massachusetts General Hospital and Harvard Medical School, Boston, Massachusetts 02114*

Katia Parodi and Guillaume Landry

*Department of Medical Physics, Ludwig-Maximilians-Universität München, Garching bei München 85748, Germany*

(Received 12 April 2016; revised 30 August 2016; accepted for publication 5 September 2016; published 23 September 2016)

**Purpose:** This work aims at investigating intensity corrected cone-beam x-ray computed tomography (CBCT) images for accurate dose calculation in adaptive intensity modulated proton therapy (IMPT) for prostate and head and neck (H&N) cancer. A deformable image registration (DIR)-based method and a scatter correction approach using the image data obtained from DIR as prior are characterized and compared on the basis of the same clinical patient cohort for the first time.

**Methods:** Planning CT (pCT) and daily CBCT data (reconstructed images and measured projections) of four H&N and four prostate cancer patients have been considered in this study. A previously validated Morphons algorithm was used for DIR of the planning CT to the current CBCT image, yielding a so-called virtual CT (vCT). For the first time, this approach was translated from H&N to prostate cancer cases in the scope of proton therapy. The warped pCT images were also used as prior for scatter correction of the CBCT projections for both tumor sites. Single field uniform dose and IMPT (only for H&N cases) treatment plans have been generated with a research version of a commercial planning system. Dose calculations on vCT and scatter corrected CBCT (CBCT<sub>cor</sub>) were compared by means of the proton range and a gamma-index analysis. For the H&N cases, an additional diagnostic replanning CT (rpCT) acquired within three days of the CBCT served as additional reference. For the prostate patients, a comprehensive contour comparison of CBCT and vCT, using a trained physician's delineation, was performed.

**Results:** A high agreement of vCT and CBCT<sub>cor</sub> was found in terms of the proton range and gamma-index analysis. For all patients and indications between 95% and 100% of the proton dose

profiles in beam's eye view showed a range agreement of better than 3 mm. The pass rate in a (2%,2mm) gamma-comparison was between 96% and 100%. For H&N patients, an equivalent agreement of vCT and CBCT<sub>cor</sub> to the reference rpCT was observed. However, for the prostate cases, an insufficient accuracy of the vCT contours retrieved from DIR was found, while the CBCT<sub>cor</sub> contours showed very high agreement to the contours delineated on the raw CBCT.

**Conclusions:** For H&N patients, no considerable differences of vCT and CBCT<sub>cor</sub> were found. For prostate cases, despite the high dosimetric agreement, the DIR yields incorrect contours, probably due to the more pronounced anatomical changes in the abdomen and the reduced soft-tissue contrast in the CBCT. Using the vCT as prior, these inaccuracies can be overcome and images suitable for accurate delineation and dose calculation in CBCT-based adaptive IMPT can be retrieved from scatter correction of the CBCT projections. © 2016 American Association of Physicists in Medicine. [<http://dx.doi.org/10.1118/1.4962933>]

Key words: proton therapy, cone-beam CT, adaptive radiotherapy

## 1. INTRODUCTION

Due to its favorable physical properties, external beam radiotherapy with proton beams plays an increasingly important role in the treatment of localized tumors.<sup>1</sup> Advanced beam delivery techniques with active magnetic scanning of narrow pencil beams<sup>2</sup> enable highly conformal dose shaping in intensity modulated proton therapy (IMPT). This allows for an increased dose to the tumor at a reduced integral dose to the normal tissue and organs at risk (OAR) with respect to conventional photon therapy. Two of the indications potentially benefiting from the more conformal dose distributions in IMPT are tumors in the head and neck (H&N) region,<sup>3-5</sup> as well as tumors of the prostate.<sup>6-8</sup> However, enhanced conformity comes along with an increased sensitivity to anatomical variations during the course of fractionated treatment.<sup>9-11</sup> For H&N tumor patients, particularly weight-loss but also tumor shrinkage can lead to considerable anatomical changes on a time scale of days to weeks.<sup>12</sup> For prostate cancer patients, changes in bladder and rectum filling, also impacting the position of the clinical and planning target volumes (CTV, PTV), can evolve within hours or even minutes, such that the patient anatomy might strongly vary from fraction to fraction.<sup>13,14</sup>

In order to fully exploit the promised advantages of IMPT, it is thus highly desirable to properly react to such interfractional changes, leading to the concept of adaptive radiotherapy (ART), where the treatment plan is frequently adapted, i.e., reoptimized, on the basis of the actual patient anatomy.<sup>15-17</sup> A pre-requisite for the implementation of ART is the availability of frequent 3D computed tomography (CT) imaging data allowing for accurate dose calculation. Consequently, most studies on image-guided ART still deal with conventional photon radiotherapy, where dose calculation depends less on the accuracy of CT numbers and where 3D imaging data are more frequently available due to the clinical usage of linac-mounted cone-beam CT (CBCT) for patient alignment. However, recently more and more proton therapy system vendors equip their gantries with CBCT imaging systems intended for patient positioning.<sup>18,19</sup> The acquired CBCT images provide information on the position of bony anatomy, the gross volume changes, and the position of the patient on

the treatment couch. But among other aspects, due to the high scatter contribution,<sup>20</sup> image quality is typically insufficient for accurate dose calculation in IMPT, even if rescaling the image intensities.<sup>21</sup> Nevertheless, several groups have recently shown that CBCTs can be used for reliable proton dose calculation by utilizing deformable image registration (DIR) of the planning CT (pCT) to the daily CBCT, yielding a so-called virtual CT (vCT).<sup>22-24</sup> This approach has been comprehensively investigated and found accurate for H&N and lung cancer patient cohorts.<sup>19,25</sup> Alternatively, it has also been suggested to use the DIR-based vCT as prior for scatter correction of the CBCT projections.<sup>26,27</sup> Promising results for protons have been obtained with this method, in the following referred to as corrected CBCT (CBCT<sub>cor</sub>), using phantom data and a single prostate cancer patient case.<sup>28</sup>

In this work, we present the first application of the vCT approach to prostate cancer IMPT. Additional challenges compared to previous studies for H&N cancer patients are to be expected due to the large anatomical changes and the further reduced soft tissue contrast in the CBCT data. Moreover, this contribution features the first proton therapy oriented implementation of the CBCT scatter correction approach for clinical H&N patient data, as well as the first comprehensive comparison of vCT and CBCT<sub>cor</sub> using the same clinical cohort of H&N and prostate cancer patients. Eventually, we aim at comparing the accuracy of these two methods for their application in CBCT-guided adaptive IMPT and on identifying potential advantages from using the complementary information of the vCT as prior for scatter correction of the CBCT.

## 2. METHODS

### 2.A. Acquired data and patient cohort

For implementation and validation of the CBCT<sub>cor</sub> approach using the XVI 4.5.1 on-board CBCT imaging system of an Elekta Synergy linac (Elekta, Sweden) at the Radiotherapy Department of the LMU Munich, CBCT images of the following phantoms have been acquired: the standard Gammex RMI 467 phantom (Gammex, Inc., USA) used for CT calibration, an in-house small-diameter (15 cm)

TABLE I. Settings for the phantom and patient CBCT acquisitions.

Subject	Tube current (mA)	Exposure time (ms/projection)	Tube voltage (kVp)	Bowtie filter	Panel position and collimator
Alderson H&N	10	10	100	No	S20
Alderson pelvis	64	40	120	Yes	M15
Small Gammex	10	10	100	No	S20
Standard Gammex	64	40	120	Yes	M15
H&N patients	10	10	100	No	S20
Prostate patients	64	40	120	Yes	M15

cylindrical PMMA phantom where four tissue-equivalent Gammex inserts were placed next to each other in a central bore (referred to as “small Gammex”), and the H&N section as well as the pelvic section of the Alderson phantom (RSD, Inc., USA). The settings of the CBCT acquisitions are shown in Table I. For each phantom, also a reference diagnostic CT was acquired at 120 kVp with a Toshiba Aquilion LB scanner (Toshiba Medical Systems, the Netherlands). CBCT images were reconstructed on a  $1 \times 1 \times 1 \text{ mm}^3$ , diagnostic CTs on a  $1 \times 1 \times 3 \text{ mm}^3$  grid.

For evaluation of vCT and  $\text{CBCT}_{\text{cor}}$  in a clinical setting, pCT data (acquired on the same Toshiba scanner) and CBCT data, i.e., reconstructed images and measured projections, of four H&N (HN1-4) and four prostate cancer patients (PR1-4) originally treated with IMRT at the Radiotherapy Department of the LMU Munich were included in this study. No contrast agent was applied for all scans considered in this work. Three of the H&N patients suffered from tumors of the larynx or pharynx, with CTVs (including lymph nodes) extending from below the optical system to the region between the shoulders, while one H&N patient (HN2) had a lesion in the nasal cavities and a CTV reaching up to the optical system. For the four prostate cancer cases, only the high dose PTV encompassing the prostate was considered in this study, neglecting the low dose PTV following the lymphatic pathways. The CBCT scans were performed between 22 and 48 days after the initial pCT for the H&N, and between 9 and 18 days after the pCT for the prostate patients. For all H&N patients, an additional replanning CT (rpCT) was acquired within three days of the respective CBCT. The image reconstruction settings were the same as for the phantom data. The CBCT acquisition parameters are given in Table I. The pCT and rpCT of patients HN1-4 were delineated by a single trained physician, just as the pCT, CBCT, and  $\text{CBCT}_{\text{cor}}$  of patients PR1-4.

## 2.B. DIR and vCT

A Morphons algorithm,<sup>29</sup> being part of the MATLAB (Mathworks, USA) package REGGUI, was used for 3D DIR of the pCT to the respective CBCT for generating the vCT. This algorithm is known to show a reduced sensitivity to absolute image intensities, as using a metric based on the local image phase. In the applied multiscale registration approach, the retrieved deformation field is regularized by convolution with a

normalized Gaussian kernel of 1.2 voxel standard deviation at each iteration. Details on the implementation and specification of the DIR settings that were used for registration also in this study can be found in Landry *et al.*<sup>25</sup> The only modification was to allow for rotations in the initial rigid alignment of the pCT to the daily CBCT, mimicking a modern six degrees-of-freedom patient couch. For the H&N patients, rigid alignment was performed automatically in a manually defined region of interest (ROI) around the spine containing the first to sixth vertebrae. Due to the limited accuracy of the automated initial rigid alignment found for the prostate cases, initial registration was performed manually for these patients, focusing on the bony anatomy in close vicinity to the CTV.

For all patients, a threshold-based cavity filling and emptying algorithm based on a comparison of image intensities in the vCT and the original CBCT, as discussed in Landry *et al.*,<sup>25</sup> was applied after DIR. All retrieved vCTs were transformed to the same workspace (i.e., same position and voxel-grid) as the initial pCT for further evaluation. Regions outside the CBCT field-of-view (FOV) in the vCT were stitched with the pCT. Due to the smaller FOV, this was, however, only found necessary for the H&N cohort. For the prostate cohort, a half-panel shift during CBCT acquisition, as specified in the clinical protocols, allowed for extending the FOV. The obtained deformation field was also used to warp the initial pCT contours to the vCT. A comprehensive validation of the retrieved contours for H&N cases can be found in a previous study.<sup>25</sup>

## 2.C. Implementation of $\text{CBCT}_{\text{cor}}$

The generated vCTs were directly used as prior for scatter correction of the CBCT projections, following closely the approach outlined in Park *et al.*<sup>28</sup> and Niu *et al.*<sup>26</sup> In the following, the most important steps are summarized:

1. Primary beam projections ( $I_{\text{pri}}$ ) are retrieved by forward projection of the vCT according to the given cone-beam geometry using the open source reconstruction toolkit (RTK).<sup>30</sup> Projections were 512-by-512 pixels, with pixel size of 0.8 mm.
2. The raw CBCT projections ( $I_{\text{raw}}$ ) are scaled with a calibration factor (CF) to match the intensities of the primary projections.
3. The scatter contribution ( $I_{\text{sca}}$ ) in  $I_{\text{raw}}$  is estimated by subtracting the presumably scatter-free vCT projections from the scaled raw projections and subsequent

application of a smoothing operation  $f$ ,

$$I_{\text{sca}} = f(\text{CF} \times I_{\text{raw}} - I_{\text{pri}}). \quad (1)$$

4. The scatter corrected projections ( $I_{\text{cor}}$ ) are obtained from subtraction of the estimated scatter from the scaled raw CBCT projections,

$$I_{\text{cor}} = \text{CF} \times I_{\text{raw}} - I_{\text{sca}}. \quad (2)$$

5. The scatter corrected CBCT<sub>cor</sub> is generated using a standard FDK algorithm from RTK for reconstruction of the scatter corrected projections. Hann windowing was applied during reconstruction in the two directions of the projections with a cutoff equal to the Nyquist sampling frequency. Additionally, the corrected projections were smoothed by a 2D median filter with a size of 3-by-3 pixels prior to reconstruction and reconstructed images by a 1D median filter of 3 pixels applied in the superior–inferior direction.

In our implementation, we used the same smoothing function  $f$  described in Niu *et al.*<sup>26</sup> (2D median filter with 25-by-25 pixels width, followed by a Gaussian filter of 1.5 pixels standard deviation). The generous smoothing in step three ensures that the scatter correction predominantly accounts for slowly varying contributions to the projections, such as the signal from scatter and not for high frequency differences between vCT prior and CBCT caused by anatomical variations. This is essential, since the vCT would be obtained if no smoothing was applied. The CF mainly accounting for differences in the mAs during CBCT acquisition was calculated as the ratio of the given CBCT acquisitions mAs and a reference value mAs<sub>ref</sub>. After careful initial optimization (see Sec. 3), the same mAs<sub>ref</sub> of 2.56 mAs, as suggested by Park *et al.*,<sup>28</sup> was used in this study. Eventually, the reconstructed CBCT<sub>cor</sub> was transferred to the pCT workspace by applying the inverse of the initial rigid pCT to CBCT alignment. Delineation of the original and scatter corrected CBCT was performed in pCT workspace for improved consistency during data analysis.

## 2.D. Treatment planning

A research version of the commercial treatment planning system RayStation (RaySearch, Sweden) was used for treatment plan generation. For patients HN1-4, IMPT plans were generated on basis of the pCT, following the constraints for parotid glands, brain stem, spinal cord, and optical system outlined in Kurz *et al.*<sup>21</sup> A constant proton relative biological effectiveness (RBE) of 1.1 was assumed throughout this study. All dose values will be given in terms of RBE-weighted dose. For patients HN1 and HN3-4, four beam angles (45°, 90°, 270°, and 315° on the International Electrotechnical Commission scale, with 90° and 270° blocked in the shoulder region) were used, while for patient HN2 with a more cranial lesion a three-field arrangement was chosen [0° (blocked in the nasal/buccal cavity), 100°, and 260°]. The dose to the delineated PTVs was adopted from the prescriptions of the original clinical

simultaneous integrated boost (SIB) photon plans with two dose levels of 50.4–56.0 Gy in the low and 56.0 to 64.0 Gy in the high dose PTV.

Moreover, single field uniform dose (SFUD) distributions were generated for patients HN1-4 (on basis of the available rpCT) and PR1-4 (on basis of the pCT), using the gantry angles shown in Table IV, in order to assess the proton range in beam's eye view (BEV). For patients HN1-4, the SFUD plans targeted only the high dose PTV at the respective dose level. In the case of the prostate patients, all plans were optimized to a median target dose of 60.0 Gy and mimic a clinical treatment with alternating fields.

For initial validation of the CBCT<sub>cor</sub> implementation for the LMU Munich CBCT system, SFUD plans were also generated for the H&N (at 0° gantry angle) and prostate (at 90° gantry angle) Alderson phantom using a manually defined PTV within the phantom.

## 2.E. Data analysis

To determine the optimal mAs<sub>ref</sub> for calculation of CF, the data of the small Gammex phantom were used. For each of the four inserts (lung, adipose tissue, solid water, and cortical bone), the edge-spread function (between insert and surrounding PMMA cylinder) was determined for CBCT<sub>cor</sub> reconstructions using various mAs<sub>ref</sub>, and the difference to the edge-spread function of the reference diagnostic CT scan was determined. For further validation following the mAs<sub>ref</sub> optimization, CT numbers in the CT and CBCT<sub>cor</sub> images of the small and standard Gammex phantom were compared in the four different tissue inserts.

In addition, SFUD plans generated on the CT scans of the H&N and pelvis Alderson were recalculated on the corresponding CBCT<sub>cor</sub> and compared in terms of the proton range in BEV. The proton range was defined as the distance between the point where the considered dose profile enters the outer contour of the phantom and the distal 80% dose fall-off. Only profiles exhibiting a maximum dose of at least 50% of the prescription were considered for range analysis. The percentage of profiles with a range agreement of better than 3 and 2 mm was determined, together with the median value and half the 2.5% to 97.5% interpercentile range (IPR) of the range difference distribution.

A similar analysis was performed using the SFUD plans generated on the patient pCT (PR1-4) or rpCT (HN1-4) data. All plans were recalculated on the respective vCT and corresponding CBCT<sub>cor</sub>. Then, the same analysis in BEV was performed, comparing the proton range on the vCT and CBCT<sub>cor</sub> for all patients. For patients HN1-4, an additional range-based comparison of vCT and CBCT<sub>cor</sub> with the rpCT was carried out. The latter might serve as a reference since it was acquired within three days of the CBCT and since most changes appear over longer time scales for H&N patients. The IMPT plans optimized on the pCT for patients HN1-4 were also recalculated on vCT, CBCT<sub>cor</sub>, and rpCT. The retrieved dose distributions have been compared to each other using a gamma-index analysis<sup>31,32</sup> with a (3%, 3 mm) and (2%, 2 mm) criterion. For the prostate cases, the SFUD plans on vCT and CBCT<sub>cor</sub> have

been compared in the same way. Only voxels with at least 50% of the prescribed dose were included in the gamma evaluation.

To assess the accuracy of the performed DIR in the pelvic region, the contours obtained from DIR of the pCT to the CBCT have been compared to the contours drawn by a trained physician on the raw CBCT. As parameters, the dice similarity coefficient (DSC), the Hausdorff distance (HD) and the mean, as well as the HD<sub>95</sub> of the contour distance distribution have been considered. In this context, HD<sub>95</sub> is defined such that 95% of the values in the contour distance distribution are smaller than HD<sub>95</sub>. The same measures were used to compare the contours delineated by the same physician on the CBCT<sub>cor</sub> to those of the raw CBCT.

### 3. RESULTS

#### 3.A. Validation of CBCT<sub>cor</sub> implementation

Results of the mAs<sub>ref</sub> optimization for the four different inserts of the small Gammex phantom are shown in Table II. For every insert, the mAs<sub>ref</sub> yielding the CBCT<sub>cor</sub> with the smallest standard deviation to the diagnostic CT is shown. Values range from 2.24 mAs in bone to 2.75 mAs in solid water. Due to the shallow minimum found in the mAs<sub>ref</sub> optimization, a value of 2.56 mAs, as suggested in Park *et al.*,<sup>28</sup> was used in this study. The Hounsfield units (HU) in the four different inserts are compared for the CBCT<sub>cor</sub>, using the optimized mAs<sub>ref</sub>, and the reference diagnostic CT in Table III. For the small and the standard Gammex phantom, we found an agreement within one sigma for all inserts. Deviations in terms of the corresponding attenuation coefficients were below 3%. In Fig. 1, the SFUD plans optimized on the reference pCT and recalculated on the CBCT<sub>cor</sub> are shown for the H&N and pelvic section of the Alderson phantom. For the pelvic section, the range analysis showed 100% of the profiles in BEV agreeing within 2 mm, at a median range difference (RD) of only -0.4 mm and an IPR of 0.7 mm. Analysis for the H&N section resulted in 93% of the profile within 3 mm and 86% within 2 mm range difference. The median difference was 0.3 mm and the IPR 3.0 mm. The reduced agreement for the H&N section could be attributed to slight differences in the position of the Alderson phantom slabs in the registered CT and CBCT images, as well as to the relatively large air gaps in between, with respect to the pelvic section.

#### 3.B. Comparison of vCT and CBCT<sub>cor</sub>

The pCT, uncorrected CBCT, CBCT<sub>cor</sub>, vCT, and reference rpCT (only for H&N case) are compared in Fig. 2 for patients

TABLE II. Results of the mAs<sub>ref</sub> optimization for the four considered inserts. In the work of Park *et al.*, a value of 2.56 mAs was empirically derived from repeated scans of a pelvic phantom at different mAs.

Insert	Lung	Adipose tissue	Solid water	Cortical bone
mAs <sub>ref</sub> (mAs)	2.61	2.57	2.75	2.24

TABLE III. HU comparison of diagnostic CT and CBCT<sub>cor</sub> for the four different inserts in the small and standard Gammex phantoms. Mean value and standard deviation are given.

Phantom	Insert	HU CT	HU CBCT <sub>cor</sub>
Small Gammex	Lung	-588 ± 18	-585 ± 36
	Adipose tissue	-114 ± 3	-104 ± 31
	Solid water	4 ± 3	15 ± 32
	Cortical bone	1517 ± 12	1481 ± 94
Standard Gammex	Lung	-562 ± 19	-571 ± 34
	Adipose tissue	-101 ± 16	-93 ± 50
	Solid water	-9 ± 16	0 ± 42
	Cortical bone	1249 ± 17	1317 ± 96

HN3 and PR1. The rpCT of patient HN3 indicates considerable weight-loss and tumor shrinkage during treatment, leading to considerable changes in the patient outline compared to the pCT (see also difference image in the second row of Fig. 2). These changes are consistently present in both CBCT images and the vCT. While the raw CBCT exhibits clearly increased CT numbers, the CBCT<sub>cor</sub> intensity level is similar to the vCT and rpCT, while exhibiting a slightly increased noise level. Differences of the corrected images to the rpCT appear mainly at the bones and air cavities due to suboptimal alignment. A perfect registration throughout the extended irradiated area is not feasible because of patient repositioning. For patient PR1, anatomical changes with respect to the pCT, particularly in the rectum, the femurs, and the outer contour, are present in the CBCT and CBCT<sub>cor</sub>. Again, the CBCT scatter correction recovers the correct image intensities at an increased noise level. As illustrated in Fig. 3, the DIR corrected mismatches in the outer contour and the bony anatomy between the pCT and the CBCT during vCT generation. Additionally, the cavity correction appears to have been successful in modeling the changes in rectal filling.

The dose distributions of the SFUD plans, calculated on the vCT, CBCT<sub>cor</sub>, and reference rpCT (only for H&N cases) are shown for the same two patients in Figs. 4 and 5. A good agreement in terms of the proton range is indicated for

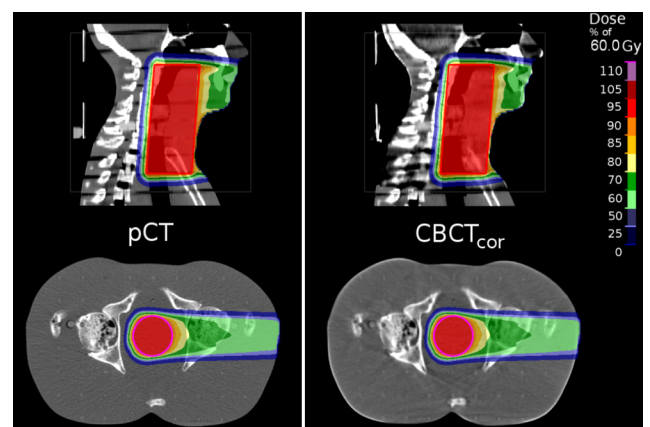


FIG. 1. SFUD plan dose distributions on the reference diagnostic pCT (left) and the CBCT<sub>cor</sub> (right) for the H&N (top) and the pelvic (bottom) section of the Alderson phantom.

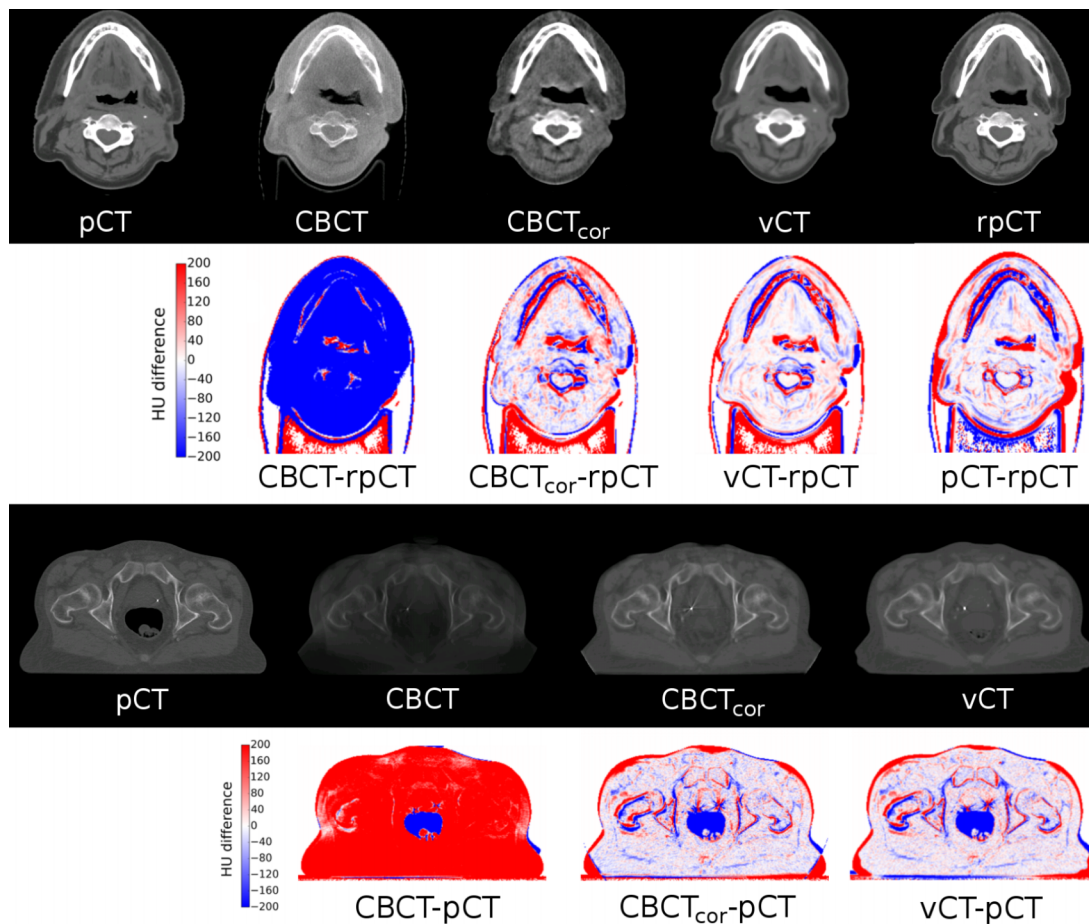


FIG. 2. pCT, raw CBCT,  $CBCT_{cor}$ , and vCT for patients HN3 (top row) and PR1 (third row). Data are shown using the same window for each image of a single patient. Difference images of pCT and rpCT, as well as CBCT,  $CBCT_{cor}$ , vCT, and rpCT are shown for patient HN3 in the second row. For patient PR1, difference images of raw CBCT,  $CBCT_{cor}$ , vCT, and pCT are shown in the bottom row.

both cases by the color-wash dose display. The quantitative results of the proton range analysis are given in Table IV. For patients PR1-4, we determined a high agreement of the proton ranges in vCT and  $CBCT_{cor}$ , with at least 95% of the BEV profiles within 3 mm and at least 90% within 2 mm. The median range difference was found below 0.5 mm, with the IPR below 1.7 mm. A comparable agreement of vCT and  $CBCT_{cor}$  was obtained for patients HN1-4. 91%–99% of the profile agreed within 2 mm, the median range difference was below 0.5 mm and IPR below 2.2 mm.

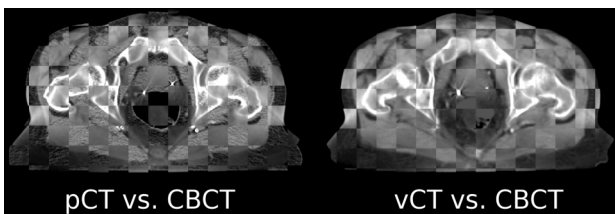


FIG. 3. Checkerboard display of pCT (left) and vCT (right) vs CBCT for patient PR1 (same slice as shown in Fig. 2). The CBCT window and level were adjusted for improved visibility. The CBCT appears brighter in the squares at the outer contour. vCT and CBCT are slightly blurred due to resampling to the pCT workspace.

Comparison of vCT and  $CBCT_{cor}$  to the reference rpCT showed a slightly reduced agreement. However, for all investigated cases, more than 90% of the BEV profiles showed a range difference of less than 3 mm and more than 80% an agreement better than 2 mm. With respect to the reference rpCT, a similar agreement of vCT and  $CBCT_{cor}$  was found, except from patient HN2, where the vCT shows improved results.

Table V summarizes the results of the gamma-index analysis of the H&N IMPT and the prostate SFUD dose distributions. Comparing vCT and  $CBCT_{cor}$ , pass rates were between 98% and 100% for a (3%,3 mm) criterion and between 96% and 100% for a (2%,2 mm) criterion. Due to the less complex field shape, agreement was slightly higher for the prostate cases. Similarity to the reference rpCT was reduced for the vCT and  $CBCT_{cor}$ , which both showed an equivalent agreement with the rpCT. Patient HN4 showed low pass rates for the vCT and  $CBCT_{cor}$  when being compared to the rpCT dose calculation.

### 3.C. Prostate contour evaluation

Despite the satisfying agreement in terms of proton range and dose distribution gamma evaluation as well as outer

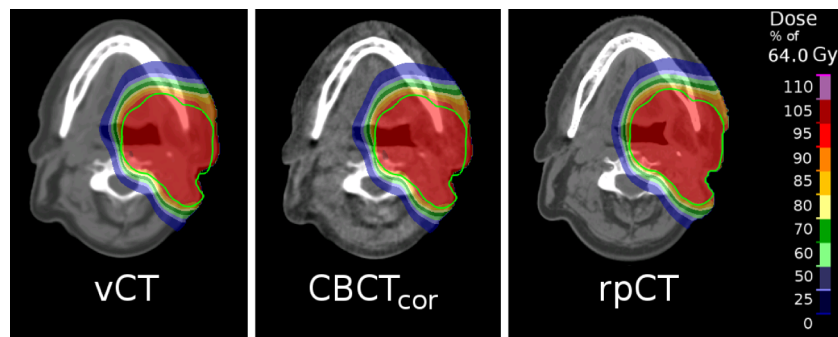


FIG. 4. SFUD plan dose distributions on the vCT (left), the  $CBCT_{cor}$  (middle), and the reference rpCT (right) for patient HN3. The PTV is depicted in green. (See color online version.)

contour and bony anatomy alignment, visual inspection of the vCT images and corresponding contours warped by the DIR from the pCT to the vCT hinted at inaccuracies for organs with large deformations in the prostate vCT images. To identify potential shortcomings in the DIR, the raw CBCT contours served as reference and were compared to the  $CBCT_{cor}$  and vCT ones. The results for the PTV, CTV, bladder, and rectum are presented in Table VI. For all considered contours and patients, the  $CBCT_{cor}$ -based contours showed an equivalent (patient PR4, PTV, and CTV) or, in most cases, an improved agreement with the reference raw CBCT contours. This can be inferred from the increased DSCs, the reduced HD, as well as the smaller mean and  $HD_{95}$  of the contour distance distribution with respect to the vCT contours. The  $CBCT_{cor}$  contours typically show a DSC in the order of 0.9 for all structures and a mean distance of below 2 mm, while the vCT DSCs can be as small as 0.63 and the mean distance as large as 8.4 mm. In contrast to the  $CBCT_{cor}$ , the vCT contours exhibit more pronounced differences for the bladder and the rectum with respect to the CTV and PTV. In these two organs, the largest HDs can also be found.

Figure 6 depicts the exemplary case of the bladder of patient PR3. pCT, vCT, raw CBCT, and  $CBCT_{cor}$  are shown together with the corresponding bladder contours. The bladder is considerably enlarged on the daily CBCT with respect to the initial pCT. The DIR could not accurately follow these changes and the vCT exhibits a bladder of similar shape as the pCT. Despite the incorrect vCT prior, the scatter corrected CBCT restores the correct shape of the bladder and enables accurate delineation in good agreement to the raw CBCT (see Table VI, DSC increased from 0.84 to 0.94). However, slightly reduced CT numbers can still be identified on the  $CBCT_{cor}$  in the anterior part of the bladder due to the inaccurate vCT

prior. To quantify the impact on the proton range, a SFUD plan at  $0^\circ$  gantry angle fully crossing this artifact region was generated for an artificial target, and the range was compared to a calculation on the  $CBCT_{cor}$  image where the content of the bladder contour was overwritten with the constant density of urine as determined from the pCT. Range differences between the two scenarios were below 1 mm for all BEV dose profiles.

As a consequence of the contour differences of vCT and  $CBCT_{cor}$ , and due to the fact that the dose distributions are very similar (see gamma-index analysis), the dose-volume-histograms (DVH) can be considerably different, as shown in Fig. 7. While for patients PR1-2, the main differences between planning scenario and daily dose distribution (decreased target coverage, reduced dose to the rectum and increased dose to the bladder) are captured in a similar way by the vCT and  $CBCT_{cor}$ -based dose evaluations, this is not the case for patients PR3-4. In the latter two cases, the vCT is close to the initial planning scenario and is not able to correctly indicate the dosimetric deviations due to the interfractional anatomical changes in the patient, as indicated by the dose evaluation on the  $CBCT_{cor}$ .

#### 4. DISCUSSION

After thorough phantom-based validation of the implementation of the CBCT projection scatter correction approach using a DIR-based vCT prior, this work presented the first application of this method to a clinically relevant IMPT scenario with four H&N and four prostate cancer patients, including a comprehensive dosimetric comparison to the vCT method. The latter was evaluated in the context of prostate proton therapy for the first time. Initial validation proved that a straight-forward implementation of the  $CBCT_{cor}$  with the same  $mAs_{ref}$  as given in Park *et al.*<sup>28</sup> is feasible when using the same Elekta on-board imaging system. The method could easily be applied to patient data. Due to vendor specific processing and storing of the CBCT projections, transfer to other on-board imaging systems might demand prior  $mAs_{ref}$  optimization, e.g., using the edge-spread function at insert boundaries as described in this work. The data for the cortical bone insert of the standard and small Gammex phantoms (Table III) suggest that the  $CBCT_{cor}$  CT numbers are more consistent with respect to beam hardening from the object than those from the pCT.

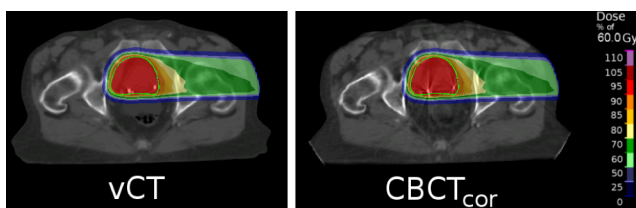


FIG. 5. SFUD plan dose distributions on the vCT (left) and the  $CBCT_{cor}$  (right) for patient PR1. The PTV is depicted in green. (See color online version.)

TABLE IV. SFUD BEV range comparison for different CT sets. The gantry angle of the considered SFUD plan, the percentage of BEV profiles with range differences (RDs) below 2 and 3 mm, the median range difference, and IPR of the range difference distribution are given. The gantry angle is according to the IEC scale.

Patient	CT sets	Angle	RD < 3 mm (%)	RD < 2 mm (%)	Median RD (mm)	IPR (mm)
PR1	vCT vs CBCT <sub>cor</sub>	90	100.0	100.0	0.2	0.6
PR2		90	99.9	99.7	0.5	0.8
PR3		90	95.4	89.7	0.1	1.7
PR4		90	100.0	99.3	0.3	1.0
HN1	vCT vs CBCT <sub>cor</sub>	315	99.7	98.9	0.1	1.1
HN2		0	97.3	91.3	0.0	2.2
HN3		90	99.5	98.8	0.1	0.8
HN4		270	99.8	99.2	0.3	1.1
HN1	rpCT vs vCT	315	95.6	91.6	-0.3	2.6
HN2		0	96.0	93.7	-0.3	2.0
HN3		90	93.0	81.5	-0.5	2.9
HN4		270	95.8	86.0	-0.5	2.8
HN1	rpCT vs CBCT <sub>cor</sub>	315	96.1	91.9	-0.3	2.4
HN2		0	94.3	86.5	-0.3	2.9
HN3		90	91.9	80.7	-0.5	3.2
HN4		270	94.2	85.2	-0.2	3.0

However, it should be kept in mind that the standard and small Gammex phantoms were scanned with different CBCT settings including kVp and bowtie filtration. Thus the results are most likely due to residual inaccuracies following the scatter correction procedure.

Overall, we found a very high agreement in terms of the proton range, inferred from dedicated SFUD plans, and the shape of the calculated proton dose distributions, inferred from a gamma-index analysis, on the vCT and CBCT<sub>cor</sub> for all H&N and prostate cancer patients. In most cases, a gamma-index pass rate of 98% or higher [using a (2%,2 mm) criterion] and an amount of more than 98% of the BEV profile ranges within 2 mm were found. For the prostate cases, only patient PR3 showed a reduced range agreement of vCT and CBCT<sub>cor</sub>. This finding could be attributed to differences in the rectum, which moved into the treated volume when recalculating the pCT-optimized plan on the vCT and CBCT<sub>cor</sub>. The cavity correction applied to the vCT overwrites regions of low CT numbers in the raw CBCT by air, i.e., -1000. As a consequence, the resulting vCT exhibited lower CT numbers than the

CBCT<sub>cor</sub> in some parts of the rectum. Cavity correction is thus potentially underestimating the CT numbers. A future refinement of the cavity correction algorithm might improve the range agreement of vCT and CBCT<sub>cor</sub>.

For the H&N cohort, comparison to a reference diagnostic rpCT confirmed the equivalent performance of both algorithms in the scope of IMPT. In general, agreement between vCT and CBCT<sub>cor</sub> was higher than agreement of any of these two methods with the reference rpCT. This is due to the fact that the rpCT has been taken after repositioning the patients on a different day. In particular, movements in the neck and differences in the shoulder position were identified to reduce the agreement to the rpCT, which might thus not always serve as an optimal ground truth. This was found most pronounced for patient HN4, showing the lowest gamma-index pass rate, which was further reduced by changes in the oral cavity. Since the SFUD plans were optimized to cover only the smaller high dose PTV located in the neck region, effects on the SFUD range were less critical for this patient. Only in a single case, patient HN2, a slightly improved range agreement of vCT

TABLE V. Gamma-index pass rates in percent for H&N IMPT and prostate SFUD dose distributions. The compared CT sets are given with the corresponding pass rates for a (3%,3 mm) and (2%,2 mm) gamma-criterion.

Patient	vCT, rpCT	CBCT <sub>cor</sub> , rpCT	CBCT <sub>cor</sub> , vCT	vCT, rpCT	CBCT <sub>cor</sub> , rpCT	CBCT <sub>cor</sub> , vCT
	(3%,3 mm)			(2%,2 mm)		
HN1	93.1	92.5	99.2	84.2	83.6	98.3
HN2	97.7	97.6	99.8	94.4	92.7	98.3
HN3	94.4	95.4	98.1	87.6	89.0	96.0
HN4	74.0	73.6	99.8	57.8	58.1	98.6
PR1	—	—	100.0	—	—	100.0
PR2	—	—	100.0	—	—	100.0
PR3	—	—	100.0	—	—	99.9
PR4	—	—	100.0	—	—	99.9

TABLE VI. Comparison of CBCT<sub>cor</sub> and vCT contours to the raw CBCT contours. The DSC, the HD as well as the mean and HD<sub>95</sub> of the contour distance distribution are given for CTV, PTV, bladder, and rectum.

Patient		CBCT <sub>cor</sub>				vCT			
		PTV	CTV	Bladder	Rectum	PTV	CTV	Bladder	Rectum
PR1	DSC	0.90	0.86	0.95	0.87	0.81	0.75	0.89	0.74
	HD	6.9	7.1	4.4	9.7	13.5	10.2	21.2	15.2
	Mean	1.7	1.8	0.9	1.4	3.5	3.7	2.4	3.1
	HD <sub>95</sub>	4.4	4.6	3.0	4.3	9.5	8.7	11.3	9.0
PR2	DSC	0.92	0.90	0.95	0.94	0.88	0.85	0.76	0.80
	HD	6.8	6.7	6.0	4.3	10.5	10.2	41.5	58.8
	Mean	1.6	1.5	1.0	0.7	2.7	2.3	6.5	6.4
	HD <sub>95</sub>	6.0	5.6	3.0	2.3	7.5	5.0	27.2	28.0
PR3	DSC	0.92	0.89	0.94	0.89	0.84	0.77	0.84	0.77
	HD	7.2	8.1	10.0	9.6	14.2	16.0	27.9	21.3
	Mean	1.3	1.4	0.9	1.4	3.1	2.9	2.7	2.6
	HD <sub>95</sub>	4.1	4.0	3.6	4.1	7.4	8.1	11.5	10.9
PR4	DSC	0.92	0.89	0.92	0.90	0.93	0.91	0.63	0.81
	HD	10.1	10.6	6.1	7.8	6.2	5.7	34.7	14.4
	Mean	1.7	1.6	1.2	0.9	1.3	1.2	8.4	1.9
	HD <sub>95</sub>	3.3	3.2	3.2	2.9	3.2	3.1	25.6	6.9

and rpCT was found with respect to the CBCT<sub>cor</sub>. This is mainly due to differences in the nasal cavity that are especially critical for the used beam angle of 0°, which would, however, typically be blocked in this region for clinical treatments. In this case, the CBCT<sub>cor</sub> exhibited slightly reduced densities in the bony structure in direct proximity of the cavities. Nevertheless, gamma-index analysis for this patient showed that for a clinically realistic three beam IMPT arrangement, differences between vCT and CBCT<sub>cor</sub> were negligible.

Considering the fact that the vCT approach and the automatically generated warped contours have been extensively validated and found sufficiently accurate in the context of IMPT<sup>25</sup> for H&N cancer, a benefit of utilizing the vCT as prior for CBCT scatter correction could not be identified. Both algorithms can be considered equivalent.

Despite negligible dosimetric differences between the two techniques, visual inspection and contour comparison proved

that the applied DIR is insufficiently accurate in the prostate region for organs with large nonrigid deformation, although the DIR generally matched the bony structures and the outer contour successfully (see difference images in Fig. 2). Similar findings, using different DIR algorithms have been reported previously.<sup>33,34</sup> In agreement with Thor *et al.*,<sup>33,34</sup> the main DIR inaccuracies were found for bladder and rectum. Both organs can be subject to considerable changes in volume and shape, which the DIR might not be able to follow. The relatively low soft tissue contrast in the CBCT images of the pelvis in combination with artifacts, such as streaks due to respiratory motion, might further undermine the DIR performance. For H&N cases, the used DIR was found to work accurately even for patients with volume changes of up to 8% in the neck region,<sup>25</sup> however, in contrast to some structures in the pelvic region, anatomical changes are still rather small and gradual. There is less relative motion of

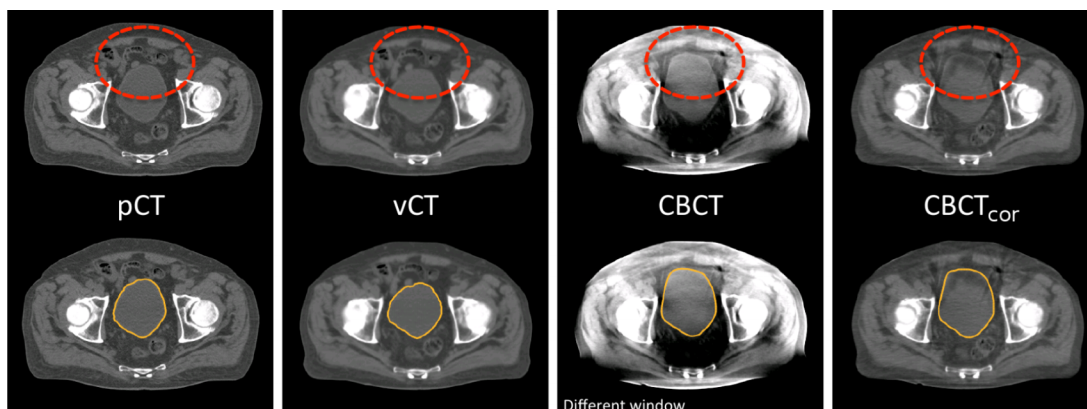


FIG. 6. Comparison of the bladder contour (bottom row) for patient PR3 on the pCT (left), vCT (second from left), the uncorrected CBCT (second from right, displayed at a different window level), and the CBCT<sub>cor</sub>. Differences between vCT and CBCT appear mainly in the anterior region of the bladder (see dashed circle, top row).

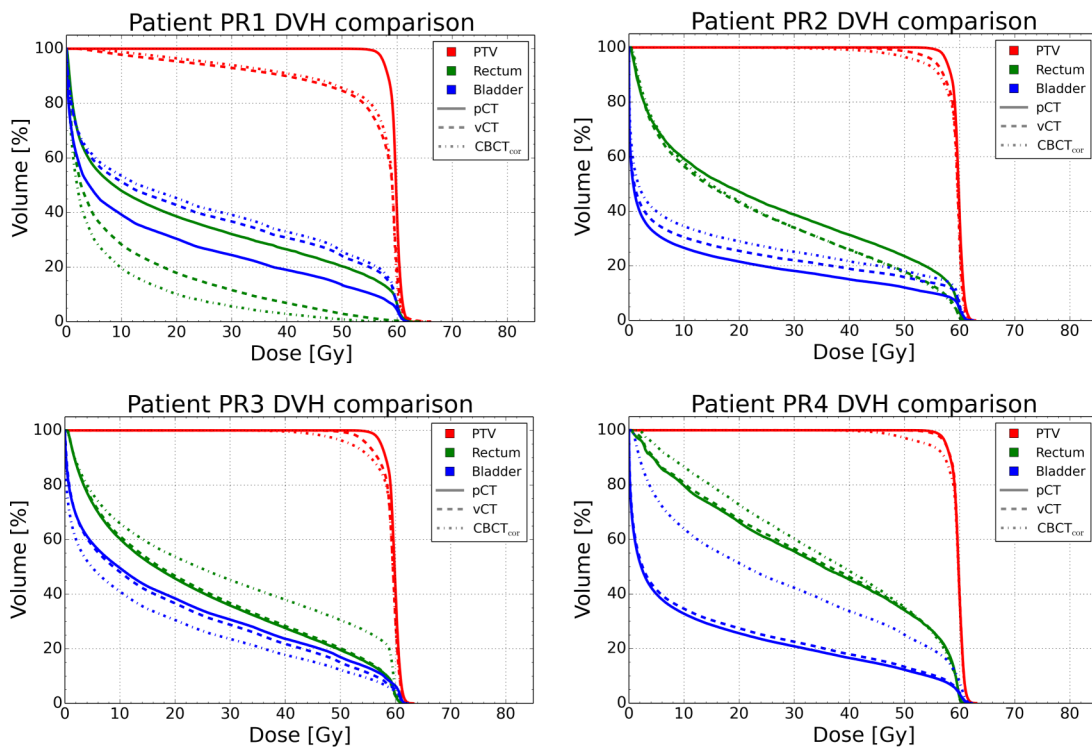


FIG. 7. DVH comparison for the prostate cases. PTV, rectum, and bladder are shown for the original pCT (solid line), the vCT (dashed line, using the vCT contours) and the CBCT<sub>cor</sub> (dotted, using the physician contours). The CTV is not shown for improved visibility.

the different structures with respect to each other. In the same publication, it was also shown that the DIR was least accurate for warping the GTV, probably since it shows a comparably low contrast with respect to the surrounding tissue, similar to, e.g., the bladder and rectum. In general, balancing out the need to follow large anatomical changes and to keep the deformation field smooth by regularization is a difficult task, which might require application of locally adapted regularization techniques, as used, e.g., in DIR of lung images.<sup>35</sup> In this work, optimization of the DIR parameters (number of iterations and scales, resolution of scales in the used multiscale DIR approach) could not improve the results. In contrast to our findings, a similar accuracy for CT to CBCT DIR accuracy in H&N and prostate has been reported by

Moteabbed *et al.*<sup>36</sup> Results in the latter study have, however, been inferred from phantom data only, using *a priori* defined deformation fields from the DIR algorithm. Moreover, rectal movement was restricted by usage of an endorectal balloon and also the extent of the bladder volume changes might have been smaller than in our study.

Nevertheless, we have shown in this work that inaccuracies in the DIR-based vCT can effectively be overcome by utilizing the vCT only as prior for CBCT scatter correction, yielding an image that exhibits the correct patient anatomy and is suitable for accurate daily dose calculation in an adaptive IMPT scenario. Due to the generous smoothing function when estimating the scatter map in the CBCT<sub>cor</sub> generation, geometrical inaccuracies of the vCT on comparably small

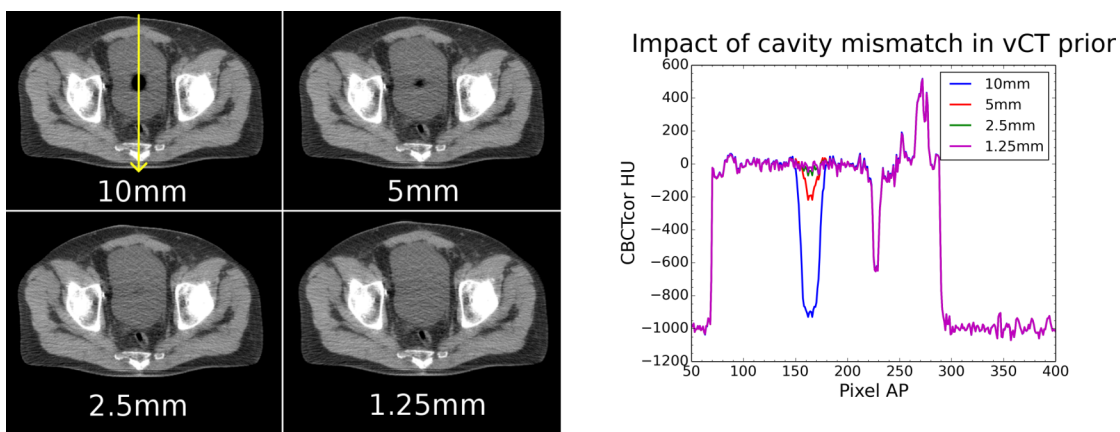


FIG. 8. Impact of a spherical cavity mismatch of various radii (see labels) in the vCT prior on the corresponding CBCT<sub>cor</sub> (left). The profiles along the depicted yellow arrow are shown on the right.

scales only marginally impact the reconstructed  $CBCT_{cor}$  image (see Fig. 6). In particular, impact on the proton range was found marginal. The same is true for inaccuracies in the cavity correction applied to the vCT prior, as discussed also by Park *et al.*<sup>28</sup> and as illustrated in Fig. 8 for an artificial air cavity of various radii introduced into the bladder on the vCT prior but not present on the raw CBCT. As can be seen, the artificial air cavity in the prior can lead to incorrect CT numbers of the  $CBCT_{cor}$ , but only if the radius exceeds a size of about 2.5 mm. In a clinical adaptive IMPT prostate treatment scenario, we would thus recommend usage of the  $CBCT_{cor}$  rather than the vCT, also since the time-consumption of additional generation of the  $CBCT_{cor}$  from the vCT prior is very small (order of minutes). Despite their limited accuracy, the vCT contours might serve as initial guess to speed-up manual contouring of the daily imaging data to eventually enable accurate dose calculation and optimization in adaptive IMPT.

At present, the time effort for DIR is still comparably high (above 10 min) and represents the main limiting factor for implementation of the investigated techniques for online IMPT treatment adaptation. In future, this issue might be overcome, e.g., by GPU DIR implementation.<sup>37</sup>

## 5. CONCLUSIONS

In this work, two techniques for CBCT intensity correction based on DIR of the pCT to the daily CBCT have been investigated and compared for the first time in terms of their usability for accurate dose calculation in the scope of adaptive IMPT. The vCT, retrieved as immediate result of the DIR, was found equivalent to the  $CBCT_{cor}$ , which uses the vCT as prior for CBCT projection scatter correction, in the case of IMPT for H&N cancer. Both methods were found suitable for accurate proton dose calculation, as required in CBCT-based adaptive IMPT. In the case of prostate cancer patients, despite negligible differences in the calculated proton dose distributions, the vCT was found insufficiently accurate on the basis of a detailed contour analysis. A main finding of this study was, however, that these inaccuracies, which particularly affect the determination of clinically relevant DVH parameters, can be largely overcome by using the vCT only as a prior for CBCT scatter correction. Thus, we consider the  $CBCT_{cor}$  an interesting approach to enable and extend the applicability of CBCT-based adaptive IMPT to sites where the accuracy of DIR might be limited, e.g., due to pronounced anatomical changes.

## ACKNOWLEDGMENTS

This work was supported by the Federal Ministry of Education and Research of Germany (BMBF), Grant No. 01IB13001 (SPARTA), and by the German Research Foundation (DFG) Cluster of Excellence Munich-Centre for Advanced Photonics (MAP). The authors thank Guillaume Janssens and Jonathan Orban de Xivry for sharing the REGGUI toolkit containing the implementation of the Morphons algorithm. Helpful advice concerning IMPT treatment planning from Silvia Molinelli,

Mario Ciocca, Barbara Knäusl, Martin Hillbrand, Daniel Köpl, and Franz Joachim Kaiser is gratefully acknowledged. The authors thank Erik Traneus from RaySearch Laboratories for his support on the RayStation TPS.

## CONFLICT OF INTEREST DISCLOSURE

The authors have no COI to report.

<sup>a)</sup> Author to whom correspondence should be addressed. Electronic mail: christopher.kurz@physik.uni-muenchen.de

<sup>1</sup> D. Marco and S. Loeffler Jay, "Charged particles in radiation oncology," *Nat. Rev. Clin. Oncol.* **7**, 37–43 (2010).

<sup>2</sup> T. Haberer, W. Becher, D. Scharadt, and G. Kraft, "Magnetic scanning system for heavy ion therapy," *Nucl. Instrum. Methods Phys. Res., Sect. A* **330**, 296–305 (1993).

<sup>3</sup> T. A. van de Water, A. J. Lomax, H. P. Bijl, M. E. de Jong, C. Schilstra, E. B. Hug, and J. A. Langendijk, "Potential benefits of scanned intensity-modulated proton therapy versus advanced photon therapy with regard to sparing of the salivary glands in oropharyngeal cancer," *Int. J. Radiat. Oncol., Biol., Phys.* **79**, 1216–1224 (2011).

<sup>4</sup> J. Góra, P. Kuess, M. Stock, P. Andrzejewski, B. Knäusl, B. Paskeviciute, G. Altorjai, and D. Georg, "ART for head and neck patients: On the difference between VMAT and IMPT," *Acta Oncol.* **54**, 1166–1174 (2015).

<sup>5</sup> T. Gupta, C. Hotwani, S. Kannan, Z. Master, V. Rangarajan, V. Murthy, A. Budrukkar, S. Ghosh-Laskar, and J. P. Agarwal, "Prospective longitudinal assessment of parotid gland function using dynamic quantitative pertechnate scintigraphy and estimation of dose–response relationship of parotid-sparing radiotherapy in head-neck cancers," *Radiat. Oncol.* **10**, 1–9 (2015).

<sup>6</sup> A. Trofimov, P. L. Nguyen, J. J. Coen, K. P. Doppke, R. J. Schneider, J. A. Adams, T. R. Bortfeld, A. L. Zietman, T. F. DeLaney, and W. U. Shipley, "Radiotherapy treatment of early-stage prostate cancer with IMRT and protons: A treatment planning comparison," *Int. J. Radiat. Oncol., Biol., Phys.* **69**, 444–453 (2007).

<sup>7</sup> C. Vargas, A. Fryer, C. Mahajan, D. Indelicato, D. Horne, A. Chellini, C. McKenzie, P. Lawlor, R. Henderson, Z. Li, L. Lin, K. Olivier, and S. Keole, "Dose volume comparison of proton therapy and intensity-modulated radiotherapy for prostate cancer," *Int. J. Radiat. Oncol., Biol., Phys.* **70**, 744–751 (2008).

<sup>8</sup> N. P. Mendenhall, Z. Li, B. S. Hoppe, R. B. Marcus, Jr., W. M. Mendenhall, R. C. Nichols, C. G. Morris, C. R. Williams, J. Costa, and R. Henderson, "Early outcomes from three prospective trials of image-guided proton therapy for prostate cancer," *Int. J. Radiat. Oncol., Biol., Phys.* **82**, 213–221 (2012).

<sup>9</sup> C. Bert and M. Durante, "Motion in radiotherapy: Particle therapy," *Phys. Med. Biol.* **56**, R113–R144 (2011).

<sup>10</sup> B. S. Müller, M. N. Duma, S. Kampfer, S. Nill, U. Oelfke, H. Geinitz, and J. J. Wilkens, "Impact of interfractional changes in head and neck cancer patients on the delivered dose in intensity modulated radiotherapy with protons and photons," *Phys. Med.* **31**, 266–272 (2015).

<sup>11</sup> D. J. Thomson, B.-K. K. Teo, A. Ong, K. W. Ang, M. Kirk, P. H. Ahn, J. N. Lukens, S. Swisher-McClure, T. Liptrot, T. D. Solberg, N. J. Slevin, and A. Lin, "The impact of anatomic change on pencil beam scanning in the treatment of oropharynx cancer," *Int. J. Part. Ther.* **2**, 394–403 (2015).

<sup>12</sup> L. Barker Jerry, Jr., S. Garden Adam, Ang K. Kian, C. O'Daniel Jennifer, H. Wang, E. Court Laurence, H. Morrison William, I. Rosenthal David, Chao K. S. Clifford, L. Tucker Susan, R. Mohan, and L. Dong, "Quantification of volumetric and geometric changes occurring during fractionated radiotherapy for head-and-neck cancer using an integrated CT/linear accelerator system," *Int. J. Radiat. Oncol., Biol., Phys.* **59**, 960–970 (2004).

<sup>13</sup> K. C. Bylund, J. E. Bayouth, M. C. Smith, A. C. Hass, S. K. Bhatia, and J. M. Buatti, "Analysis of interfraction prostate motion using megavoltage cone beam computed tomography," *Int. J. Radiat. Oncol., Biol., Phys.* **72**, 949–956 (2008).

<sup>14</sup> C. Beltran, M. G. Herman, and B. J. Davis, "Planning target margin calculations for prostate radiotherapy based on intrafraction and interfraction motion using four localization methods," *Int. J. Radiat. Oncol., Biol., Phys.* **70**, 289–295 (2008).

- <sup>15</sup>G. X. Ding, D. M. Duggan, C. W. Coffey, M. Deeley, D. E. Hallahan, A. Cmelak, and A. Malcolm, "A study on adaptive IMRT treatment planning using kV cone-beam CT," *Radiother. Oncol.* **85**, 116–125 (2007).
- <sup>16</sup>J. Nijkamp, F. J. Pos, T. T. Nuver, R. de Jong, P. Remeijer, J.-J. Sonke, and J. V. Lebesque, "Adaptive radiotherapy for prostate cancer using kilovoltage cone-beam computed tomography: First clinical results," *Int. J. Radiat. Oncol., Biol., Phys.* **70**, 75–82 (2008).
- <sup>17</sup>C. B. Simone, D. Ly, T. D. Dan, J. Ondos, H. Ning, A. Belard, J. O'Connell, R. W. Miller, and N. L. Simone, "Comparison of intensity-modulated radiotherapy, adaptive radiotherapy, proton radiotherapy, and adaptive proton radiotherapy for treatment of locally advanced head and neck cancer," *Radiother. Oncol.* **101**, 376–382 (2011).
- <sup>18</sup>S. Rit, R. Clackdoyle, P. Keuschnigg, and P. Steininger, "Filtered-backprojection reconstruction for a cone-beam computed tomography scanner with independent source and detector rotations," *Med. Phys.* **43**, 2344–2352 (2016).
- <sup>19</sup>C. Veiga, G. Janssens, C.-L. Teng, T. Baudier, L. Hotoiu, J. R. McClelland, G. Royle, L. Lin, L. Yin, J. Metz, T. D. Solberg, Z. Tochner, C. B. Simone, J. McDonough, and B.-K. K. Teo, "First clinical investigation of CBCT and deformable registration for adaptive proton therapy of lung cancer," *Int. J. Radiat. Oncol., Biol., Phys.* **95**, 549–559 (2016).
- <sup>20</sup>J. H. Siewersden and D. A. Jaffray, "Cone-beam computed tomography with a flat-panel imager: Magnitude and effects of x-ray scatter," *Med. Phys.* **28**, 220–231 (2001).
- <sup>21</sup>C. Kurz, G. Dedes, A. Resch, M. Reiner, U. Ganswindt, R. Nijhuis, C. Thieke, C. Belka, K. Parodi, and G. Landry, "Comparing cone-beam CT intensity correction methods for dose recalculation in adaptive intensity-modulated photon and proton therapy for head and neck cancer," *Acta Oncol.* **54**, 1651–1657 (2015).
- <sup>22</sup>M. Peroni, D. Ciardo, M. F. Spadea, M. Riboldi, S. Comi, D. Alterio, G. Baroni, and R. Orecchia, "Automatic segmentation and online virtual CT in head-and-neck adaptive radiation therapy," *Int. J. Radiat. Oncol., Biol., Phys.* **84**, e427–e433 (2012).
- <sup>23</sup>G. Landry, G. Dedes, C. Zöllner, J. Handrack, G. Janssens, J. O. de Xivry, M. Reiner, C. Paganelli, M. Riboldi, F. Kamp, M. Sohn, J. J. Wilkens, G. Baroni, C. Belka, and K. Parodi, "Phantom based evaluation of CT to CBCT image registration for proton therapy dose recalculation," *Phys. Med. Biol.* **60**, 595–613 (2015).
- <sup>24</sup>C. Veiga, J. Alshaikhi, R. Amos, A. M. Loureno, M. Modat, S. Ourselin, G. Royle, and J. R. McClelland, "Cone-beam computed tomography and deformable registration-based dose of the day calculations for adaptive proton therapy," *Int. J. Part. Ther.* **2**, 404–414 (2015).
- <sup>25</sup>G. Landry, R. Nijhuis, G. Dedes, J. Handrack, C. Thieke, G. Janssens, J. Orban de Xivry, M. Reiner, F. Kamp, J. J. Wilkens, C. Paganelli, M. Riboldi, G. Baroni, U. Ganswindt, C. Belka, and K. Parodi, "Investigating CT to CBCT image registration for head and neck proton therapy as a tool for daily dose recalculation," *Med. Phys.* **42**, 1354–1366 (2015).
- <sup>26</sup>T. Niu, M. Sun, J. Star-Lack, H. Gao, Q. Fan, and L. Zhu, "Shading correction for on-board cone-beam CT in radiation therapy using planning MDCT images," *Med. Phys.* **37**, 5395–5406 (2010).
- <sup>27</sup>T. Niu, A. Al-Basheer, and L. Zhu, "Quantitative cone-beam CT imaging in radiation therapy using planning CT as a prior: First patient studies," *Med. Phys.* **39**, 1991–2000 (2012).
- <sup>28</sup>Y.-K. Park, G. C. Sharp, J. Phillips, and B. A. Winey, "Proton dose calculation on scatter-corrected CBCT image: Feasibility study for adaptive proton therapy," *Med. Phys.* **42**, 4449–4459 (2015).
- <sup>29</sup>G. Janssens, L. Jacques, J. O. de Xivry, X. Geets, and B. Macq, "Diffeomorphic registration of images with variable contrast enhancement," *Int. J. Biomed. Imaging* **2011**, 891585.
- <sup>30</sup>S. Rit, M. V. Oliva, S. Brousmiche, R. Labarbe, D. Sarrut, and G. C. Sharp, "The reconstruction toolkit (RTK), an open-source cone-beam CT reconstruction toolkit based on the Insight Toolkit (ITK)," *J. Phys.: Conf. Ser.* **489**, 012079 (2014).
- <sup>31</sup>D. A. Low, W. B. Harms, S. Mutic, and J. A. Purdy, "A technique for the quantitative evaluation of dose distributions," *Med. Phys.* **25**, 656–661 (1998).
- <sup>32</sup>L. C. G. G. Persoon, M. Podesta, W. J. C. van Elmpst, S. M. J. J. G. Nijsten, and F. Verhaegen, "A fast three-dimensional gamma evaluation using a GPU utilizing texture memory for on-the-fly interpolations," *Med. Phys.* **38**, 4032–4035 (2011).
- <sup>33</sup>M. Thor, J. B. B. Petersen, L. Bentzen, M. Hoyer, and L. P. Muren, "Deformable image registration for contour propagation from CT to cone-beam CT scans in radiotherapy of prostate cancer," *Acta Oncol.* **50**, 918–925 (2011).
- <sup>34</sup>M. Thor, L. Bentzen, U. V. Elstrøm, J. B. B. Petersen, and L. P. Muren, "Dose/volume-based evaluation of the accuracy of deformable image registration for the rectum and bladder," *Acta Oncol.* **52**, 1411–1416 (2013).
- <sup>35</sup>D. F. Pace, S. R. Aylward, and M. Niethammer, "A locally adaptive regularization based on anisotropic diffusion for deformable image registration of sliding organs," *IEEE Trans. Med. Imaging* **32**, 2114–2126 (2013).
- <sup>36</sup>M. Moteabbed, G. C. Sharp, Y. Wang, A. Trofimov, J. A. Efstathiou, and H.-M. Lu, "Validation of a deformable image registration technique for cone beam CT-based dose verification," *Med. Phys.* **42**, 196–205 (2015).
- <sup>37</sup>X. Gu, H. Pan, Y. Liang, R. Castillo, D. Yang, D. Choi, E. Castillo, A. Majumdar, T. Guerrero, and S. B. Jiang, "Implementation and evaluation of various demons deformable image registration algorithms on a GPU," *Phys. Med. Biol.* **55**, 207–209 (2010).